GALLIUM POLYMORPHS: PHASE-DEPENDENT PLASMONICS

*Yael Gutiérrez,[1] Maria Losurdo,[2] Pablo García-Fernández, [3] Marta Sainz de la Maza[1], Francisco González,[1] April S. Brown,[4] Henry O. Everitt[5,6] Javier Junquera[3] and Fernando Moreno[1]**

Yael Gutiérrez,[1] Dr. Maria Losurdo,[2] Dr. Pablo García-Fernández, [3] Marta Sainz de la Maza[1,3], Prof. Francisco González,[1] Prof. April S. Brown,[4] Dr. Henry O. Everitt[5,6] Dr. Javier Junquera[3] and Prof. Fernando Moreno[1]
E-mail: morenof@unican.es

Y. Gutiérrez, M. Sainz de la Maza, Prof. F. González, Prof F. Moreno
Group of Optics, Department of Applied Physics, Faculty of Sciences, University of Cantabria, Avda. Los Castros s/n, 39005 Santander, Spain

Dr. M. Losurdo
Institute of Nanotechnology, CNR-NANOTEC, via Orabona 4, 70126 Bari, Italy

Dr. P. García-Fernández, Dr. J. Junquera
Departamento de Ciencias de la Tierra y Física de la Materia Condensada, Universidad de Cantabria, Cantabria Campus Internacional, Santander, Spain

Prof. A. S. Brown
Department of Electrical and Computer Engineering, Duke University, Durham, North Carolina 27708, USA

Dr. H. O. Everitt
Department of Physics, Duke University, Durham, North Carolina 27708, USA
U.S. Army CCDC-Aviation & Missile Center, Redstone Arsenal, Alabama 35898, USA

Keywords: gallium, plasmonics, nanoparticle, phase change, polymorphism, spectroscopic ellipsometry, dielectric function

Interest in gallium (Ga) is growing rapidly, thanks in part to its wide spectral tunability and its intriguing temperature-dependent polymorphism. In order to exploit and control phase-change plasmonics in the liquid and solid phases of Ga, an accurate understanding of the dielectric functions for each Ga phase is needed. We present a comprehensive analysis of the interdependence of the crystal structure, band structure, and dielectric function of the several Ga phases (liquid, α, β, γ, δ), showing that the selective presence of flat bands in the vecinity of the Fermi energy is crucial to understand the metallicity of each phase. The dielectric function obtained through first principles calculations is compared with experimental measurements obtained by spectroscopic ellipsometry. Cooling liquid Ga always produces a mixture of phases, and we demonstrate how the volume fraction of each phase may be deduced from these pure phase dielectric functions and an analysis of the measured spectra using a Bruggeman effective medium approximation. Figures of merit are presented, and applications of Ga polymorphism are discussed for propagating and localized surface plasmon resonances in Ga thin films and nanostructures, respectively. This research can have important implications on the phase change control for plasmonics/photonic applications with gallium.

1. Introduction

Gallium is most commonly known as a liquid metal with a melting temperature just above room temperature (29.7°C). It is a non-toxic, biocompatible,[1] flexible, stretchable, and deformable metal at room temperature with low viscosity and excellent thermal and electrical conductivities[2]. However, gallium has several solid state phases, and these are receiving increasing interest for a number of reasons, chief among them being how its rich polymorphism[3–8] (see **Figure S1**) enables a variety of phase-change systems.[9–11] These systems are being developed now, even though the local structure of these phases is not well understood and the local ordering of the liquid phase is still under investigation.[12] In addition, covalent bonding of Ga dimers creates an energy dip at the Fermi level with a strong absorption band around 2.3 eV,[13] and the coexistence of metallic and covalent bonds strongly affects the metallic characteristics of the various Ga phases. Intriguingly, the coexistence of solid and liquid phases in Ga nanoparticles (NPs) can be controlled in a highly reversible and reproducible fashion, both by their epitaxial relationship with substrates[14] and by e-beam excitation.[15]

These characteristics are responsible for the unique plasmonic properties of Ga NPs, recently demonstrated to span the ultraviolet (UV), visible, and near infrared (NIR) spectral regions.[16,17] Already, Ga nanostructures have been exploited for a variety of applications, including chemical sensing (using UV surface enhanced Raman spectroscopy)[18], molecular sensing,[19] delivery of cancer therapy drugs (using transformable liquid-metal nanospheres composed of a liquid-phase gallium core and a thiolated polymeric solid shell),[1] phase-change memories,[20] reversible light-induced switching,[21] phase change nonlinear systems,[9] and "active plasmonics."[10] Many of these applications exploit changes in optical reflectivity produced by phase transformations between the various structural forms of Ga, changes stimulated by very low power (~nW) optical excitation.[22] The nature of the Ga–Ga bond is of particular interest because the way structural transformations affect optical properties may yield fascinating new mechanisms for photonic functionality, including multifunctional reconfigurable frequency- and polarization-selective surfaces.[23]

Unfortunately, the potential applicability of such Ga-based systems for photonics and plasmonics has been severely hampered by the lack of information about the optical properties of the five primary phases of Ga (liquid "*l*" and α, β, γ, δ solids), and even less is known about amalgams composed of a mixture of these phases. To date the only dielectric dispersion profiles that have been modelled are a linear combination of the liquid and α-Ga phases.[24] Since these Ga phases change with temperature, accurate knowledge of the optical response of the various Ga phases is needed for predicting and modeling the temperature dependence of Ga-containing optoelectronic devices.[25] Such phase changes are becoming even more important for predicting the plasmonic behavior of Ga when confined to nanostructures, whose high Laplace pressure and interactions with substrates[14,26,27] or solvents[28] can stabilize them into a variety of phase distribution mixtures.

Here we report a comprehensive theoretical and experimental investigation of the optical response of these four solid Ga phases, including their correlation with the respective crystalline structures and band diagrams, using dielectric functions calculated by first principles methods and experimentally validated by spectroscopic ellipsometry (a fifth solid phase, ε-Ga, is comparatively rare in nanoparticles and is not considered here). We show that α-Ga and β-Ga possess strong interband transitions at low energies while δ-Ga and γ-Ga have an almost ideal Drude-like metallic response as *l*-Ga. We demonstrate that the cooling of liquid phase Ga produces a mixture of solid phases whose distribution depends on the cooling rate and the presence of impurities. The optical properties of such mixtures can be quantitatively estimated by the volume fraction of each phase using their respective dielectric function and the Bruggeman effective medium approximation.[29] Applications of the dielectric function of the various Ga phases and their mixtures are demonstrated through the optical responses of Ga-based thin film waveguides and plasmonic Ga NPs.

2. Results and Discussion

2.1 Crystal and electronic structure of Ga phases

Figures 1a, 1d, 1g and 1j summarizes the unit cell structure for each of the four solid Ga phases. With a melting point of T_m = 302.9 K, α-Ga is the only stable phase for bulk gallium at atmosphere pressure. It crystallizes in a face-centered orthorhombic structure with space group symmetry $Cmce$ (no. 64) and a unit cell that contains eight atoms.[7,8,30] β-Ga, with a melting point of 256.8 K, is one of the metastable phases of Ga. It crystallizes in a face-centered monoclinic structure with space group symmetry $C2/c$ (no. 15) and four atoms in the unit cell.[4,7,30] γ-Ga is also a metastable phase in bulk with a similar melting point (253.8 K) but is stable at room temperature in the form of Ga NPs. It has a more complicated crystalline structure consisting of an orthorhombic unit cell with $Cmcm$ (no. 63) space group symmetry and 40 atoms in it.[5] Finally, δ-Ga, which has the lowest melting point (237.6 K), crystallizes in a rhombohedral strucuture with space group symmetry $R\bar{3}m$ (no. 166) and a unit cell that contains 22 atoms.[6]

Using density functional theory (DFT) calculations implemented on SIESTA[31] (see Methods) and minimizing the energy with standard conjugate-gradient techniques, we derived the theoretical lattice parameters and atomic positions as reported in **Table S1**. Their reliability can be assessed by the favorable comparison with experimentally obtained values also reported in the table. The densities of states (DOS), reported in Figures 1b, 1e, 1h and 1k, show an evolution from α-Ga to δ-Ga phases that goes from a very smooth DOS in this latter case, characteristic of metallic delocalized bonds, to a more jagged profile in the former case, indicating charge localization and a behavior closer to an insulating phase (dielectric character). The α-Ga DOS presents two characteristic humps above and below the Fermi energy that correspond with two nearly parallel bands associated to bonding-antibonding behavior due to covalent bonding. The electronic structure of β-Ga also exhibits some covalent behavior, its DOS also present humps above and below Fermi energy and some parallel bands along some high symmetry lines, but several other bands cross the Fermi level showing metallic behavior (see **Figure S2**). In the case of γ-Ga and δ-Ga, the DOS clearly exhibits metallic behavior since bands are continuously crossing the Fermi level although in the former a dip in the DOS close to the Fermi energy is clearly reflected in the imaginary part of the dielectric function.

Based on these band structutes and the dipolar transition matrix elements between occupied and unoccupied single-electron eigenstates, the complex dielectric function $(\epsilon(\omega) = \epsilon_1(\omega) + i\epsilon_2(\omega))$, is calculated for the different phases using first-order time-dependent perturbation theory as implemented in SIESTA[31]. The calculated complex dielectric function for each phase is shown in Figures 1c, 1f, 1i and 1l. The evolution of dielectric function spectra is clearly observed, from interband transitions in α-Ga and β-Ga below 2.5 eV to Drude-like metallic characteristics in γ-Ga and δ-Ga. Specifically, the frequency dependent complex dielectric functions of α-Ga and β-Ga manifest interband transitions ($\epsilon_1(\omega) > 0$): at 1.18 eV and 2.18 eV for α-Ga, and at 1.88 eV for β-Ga. The interband transitions responsible for these features in

$\epsilon(\omega)$, indicated with arrows in Figure S2, have been identified by evaluating the values of the optical matrix element $M_{cv\mathbf{k}}$ for every pair of conduction (c) and valence bands (v) at each $\mathbf{k}$ point along the high symmetry lines in the first Brillouin zone (see Methods). Notice that the highlighted transitions occur in the regions with parallel bands characteristic of a covalent solid. By contrast, the dielectric function of both γ-Ga and δ-Ga are very typical of good metals ($\epsilon_1(\omega) < 0$).

In **Figure 2**a, the calculated dielectric functions of α-Ga and β-Ga are compared to the reported experimental spectra of solid Ga.[32–34] The agreement above 3 eV is excellent, while the experimental results below 3 eV are intermediate between the α-Ga and β-Ga phases. The peak at ≈ 2.1 eV is attributed to the interband transition of α-Ga at 2.18 eV, while the plateau at lower energies is attributed to the contribution of the interband transitions of the α-Ga and β-Ga indicated by the dotted lines in Figure 2a. These differences suggest the experimentally measured solids were a mixture of α-Ga and β-Ga phases, especially since those reports provided no confirmation of the structural purity of the crystallographic phases. Indeed, using the dielectric function of the different phases, we may be able to estimate the contributions of each phase in each sample measured.

To demonstrate this, we have fabricated two solid Ga thin film samples under different cooling conditions (see Methods), then we measured their ellipsometric spectra and fitted them with the Bruggeman effective medium approximation (BEMA) using a volumetric weighting of two pure phases.[29] The goodness of these fits have been evaluated using the R-square coefficient of determination [35], and values for each of these fittings are gathered in **Table S2**. For comparison, in **Table S3** we show the R-square values obtained by fitting the ellipsometric spectra of both samples using the methodology used in Ref. [24]: a weighted average of α-Ga and l-Ga. By comparing both methods, the advantage of the approach proposed here becomes clear. Bruggeman effective medium approximation is the most suitable model since our samples are consituted by a completely random inhomogenous media whose components are treated symmetrically[36]. Spectroscopic measurements were performed at two locations on each sample (blue and red curves in Figures 2b and 2c), and any differences may be attributed to variability in the distribution of phase mixtures across the samples. For sample Ga#1, formed by rapidly cooling to 243K, Figure 2b shows that the spectra at both locations are nearly identical in the metallic regime above 2.5 eV. The best-fit is obtained with a BEMA mixture of 45% α-Ga : 55% β-Ga, a result is consistent with the XRD analysis (See **Table S4** in the SI). Discrepancies at lower energies (inset of Figure 2b) arise from defects, grain boundaries, and other imperfections in the sample, but the plateauing caused by interband transitions is appropriately captured. For sample Ga#2, formed by slowly cooling to 123K, Figure. 2c reveals a larger difference in the spectra measured at two locations, but they may both be reproduced with a BEMA mixture of α-Ga and γ-Ga, again consistent with XRD analysis. Interestingly, the α-phase interband transition at 2.18 eV becomes an indicator of the α-Ga to γ-Ga ratio, and the best fit of the two measured spectra reveals a ±10% variability in volume fraction of the two phases: 45% α-Ga : 55% γ-Ga for the red curve and 35% α-Ga : 65% γ-Ga for the blue curve.

From this we may conclude that the ratio of the coexisting phases may be quantitatively estimated through a simple spectroscopic analysis of Ga samples. Both the analysis of the reported experimental data and the analysis of the dielectric function of solid Ga available in literature, shows that cooling liquid Ga always produces a mixture of different phases. By fitting the experimental data with a BEMA mixture using the calculated dielectric functions, we provide a tool for estimating the composition of solid Ga films as well as the volumetric fraction of each phase in the samples.

2.2 Implications of Ga phases in plasmonic nanostructures

In order to evaluate the performance of the Ga-phases in different plasmonic systems we have theoretically analyzed two different metrics: one related to extended modes such as surface plasmon polaritons (SPPs) in thinfilms, and other related to localized surface plasmons (LSPs) in nanoparticles. In the quasistatic approxaimation, we respectively define these two quality factors as $Q_{SPP} = \epsilon_1^2/\epsilon_2$ and $Q_{LSP} = -\epsilon_1/\epsilon_2$.[37] Within this approximation, the Fröhlich energy ($\epsilon_1 = -2$) corresponds to the energy at which localized surface plasmon resonances (LSPRs) may be excited in isolated metallic particles whose size is much smaller than the incident illumination wavelength. **Figure 3** plots the spectral values of Q_{SPP} and Q_{LSP} for each of the Ga phases. The largest values of Q_{SPP} are achieved by *l*-Ga ($Q_{SPP} = 150$), δ-Ga (65), and γ-Ga (50) at energies below 2.5 eV. The more covalent solids, α-Ga and β-Ga, have much smaller Q_{SPP} values, and they fall to $Q_{SPP} = 0$ at the interband transition energies (2.18 eV for α-Ga and 1.88 eV for β-Ga). The high contrast in the values of Q_{SPP} values between *l*-, δ-, γ-Ga and α-, β-Ga below 2.5 eV points out the possibility of building plasmonic switches by the structural transformation of Ga from *l*-, δ- or γ-phases to the α- or β-phase. For each analyzed phase, Q_{LSP} exhibits a broad resonance, with a peak near 8 eV in accordance with the Fröhlich energy, except for β-Ga whose peak is near 6.5 eV. This makes Ga an excellent candidate for UV plasmonic applications, regardless of its phase. Since the more metallic phases should have greater plasmonic performance than the more covalent phases, the Q_{LSP} spectra confirm that the most efficient phase for LSPR generation is *l*-Ga, followed by δ-Ga and γ-Ga, while β-Ga and α-Ga are inferior but still retain plasmonic behavior above 2.5 eV.

Gallium layers have been used for waveguides, plasmonic switches, and phase changing devices in which α-Ga and/or l-Ga homogeneous phases were assumed.[9–11] However, considering that a pure α-Ga solid phase film cannot be achieved simply by cooling liquid Ga, we simulated the reflectance spectra of α-Ga/β-Ga and α-Ga/γ-Ga thin films by varying the content of the α-phase. **Figure 4** shows the calculated normal incidence reflectance spectra (angle of incidence AOI = 0°) of (a,b) α-Ga/β-Ga and (c,d) α-Ga/γ-Ga thin films on a sapphire substrate, calculated using the Transfer Matrix Method (TMM)[38] by varying the α-phase fraction f_α. (For normal incidence, both polarizations are equivalent. The spectra for oblique incidence (AOI =70°) and both s-/p-polarizations are shown in **Figure S3**). The dielectric function in each case has been calculated using the Bruggeman effective medium theory for mixing both phases, and the film thicknesses have been chosen to mimic the thicknesses used in actual devices (h = 20 and 150 nm (see Figures 4a,c and b,d respectively)).[9–11] It can be seen that the reflectance spectra vary significantly with h and f_α between the limits set by the pure phases, indicating that a simple spectral reflectance measurement could be used to identify the relative content of each phase in the sample. The variation with f_α for α-Ga/γ-Ga is greater because it represents a mixture of covalent and metallic phases, especially below 2.5 eV where the evolution from interband transitions in α-Ga contrasts most strongly with the metallic behavior of γ-Ga. The differences between α-Ga/β-Ga are smaller since both of them have interband transitions below 2.5 eV and metallic character above 2.5 eV.

Synthesized solid Ga nanoparticles have been reported to present the coexistence of different phases whose structural transformation can be driven by low power (≈ nW) optical excitation[22]. In order to model the plasmonic response of these NPs, and due to the lack of information on the dielectric disperssion profiles of the different Ga-phases, the optical properties of the Ga polymorphs were approximated through the linear combination of the dielectric function of *l*- and α-Ga.[22,24,39] Therefore we have simulated the plasmonic response of NPs with different geometries made of the different Ga-phases. **Figures 5**a, 5b and 5c shows the absorption cross-section spectra C_{abs} of spherical NPs and nanorods made of the different Ga phases. Both have radii of R = 10 nm, while the nanorods are L = 250 nm long. The nanorods have been illuminated along its symmetry axis and perpendicular to it (see Figures 5b and 5c, respectively). Because the nanospheres are so much smaller than the wavelengths considered, only the electric dipolar mode of each phase is observed, with an ultraviolet plasmonic resonance near 7 eV for all phases expect β-Ga, whose peak is near 6 eV. Similar results present the nanorod illuminated along its symmetry axis. In these two cases, l- and δ-Ga phases show the highest vales of C_{abs}, followed by γ-, β-, and α-Ga. The simulated excitation beam for the rods illuminated perpendiuclar to its symmetry axis was polarized 45° from it so that both longitudinal and transverse modes were excited. The intensity of each transverse plasmonic dipolar mode (near 8 eV except for β-Ga near 6.5 eV) is very similar for all phases because they each have a metallic character at these energies. On the contrary, the longitudinal mode resonances occurred below 2.5 eV where α- and β-Ga undergo interband absorption while γ-, δ-, and l-Ga remain metallic. Consequently, the C_{abs} for α- and β-Ga are lower than for the rest of the phases. It is important to point out that depending on the metallic/dielectric character of the Ga phase at the resonant energy the nature of the resonance is different. In the case of those phases with metallic behaviour (i.e., γ-, δ-, and l-Ga in all spectral range and α- and β-Ga above ≈ 2.5 eV. See Figures 1c, 1f, 1i and 1l) the resonance has a purely plasmonic nature (oscillation of the conduction electrons). However, for those phases with dielectric character ($\epsilon_1(\omega) > 0$, i.e., α- and β-Ga below ≈ 2.5 eV) the peaks are attributed to the Mie resonances whose origin comes mainly from the displacement currents inside the NPs due to the bound electrons contribution (see Figure 1 in Ref. [40]). The near-field electric field enhancement maps ($\log_{10}(|E|^2)$) shown in **Figure 5d** confirm the maximum absolute value for the longitudinal mode increases with the metallicity of the Ga-phase considered. In this way, the value of the near-field enhancement increases as Ga progresses from the α- and β- to the γ-, δ-, and l-phases.

The utility of this study becomes clear when these plasmonic structures are used for surface enhanced Raman spectroscopy (SERS) or surface enhanced fluorescence (SEF) spectroscopy in which target molecules adsorb on the surface of the NPs. **Figure 6** compares the calculated spectral absorption cross-section (C_{abs}) and near-field enhancement ($\langle|E|^2\rangle$) averaged over the surface of Ga hemispheres with radius R = 60 nm supported by a sapphire substrate and illuminated at normal incidence. The simulated geometry, plotted in Figure 6b, has been designed to mimic real Ga samples used in SERS experiments[18,41] with Ga NPs shown in the scanning electron microspy (SEM) image of Figure 6a. In general, these NPs have a solid γ-Ga core covered by a liquid shell, as was seen in transmision electron microscopy (TEM, inset of Figure 6a) previously reported in Ref. [14]. Spectroscopic signatures from adsorbed target molecules are greatest at a given photon energy when NPs have a large near-field enhancement over as much of the surface as possible. For each solid phase, each curve exhibits two resonant modes: one at low energy (between 1.5 - 2 eV which for α- and β-Ga are Mie resonances and for the rest of the phases are plasmonic modes) and another at higher energies (between 4.5 - 5 eV with a plasmonic nature for all considered phases). The low energy C_{abs} peak is blue-shifted (≈ 0.2 eV) with respect to the low energy $\langle|E|^2\rangle$ peak, but both curves share the same high energy peak. Since the values of $\langle|E|^2\rangle$ for the high energy mode are higher, it is the more appropriate mode for surface-enhanced spectroscopy. Fortuitously, a far-field measurement of this high energy resonant mode can be used to tune the laser energy to achieve the maximum near-field enhancement. Comparison of the near-field distribution of both modes reveals that the low energy mode exhibits a greater but more spatially localized enhancement, while the high energy resonant mode is slighly weaker but more evenly distributed above the surface. Thus, this high energy mode is advantageous for surface enhanced spectroscopy, since the location of the molecules on the surface is not as critical, while the low energy mode produces hot spots localized at the interface with the support and requires target molecules to be placed precisely to achieve maximum enhancement.

3. Conclusions

In summary, we report the first detailed analysis of the optical properties of the different α-, β-, γ- and δ-Ga phases and its correlation with their crystalline and electronic structures. It is found that there are significant differences in the dielectric function of the various Ga polymorphs, especially in the spectral region below 2.5 eV, with interband transitions in α- and β-Ga and Drude metallic behavior for γ-Ga and δ-Ga. Until present, although the different phases have been identified in confined systems (nanostructures), the lack of information on the dielectric dispersion of the different Ga-phases has hampered the accurate electromagnetic modelling of this Ga nanostructures, pushing experimentalists to approximate the optical constants as linear combinations of the liquid and solid (α-Ga) phase[22,39]. Furthermore, we demonstrate that optical constants attributed to α-Ga in the literature[9], obtained by supercooling *l*-Ga, actually corresponds to the mixture of α- with other Ga phases. XRD analysis of our thin film samples, shows that cooling *l*-Ga always produces a mixture of different phases, either α-/β-Ga or α-/γ-Ga depending on the cooling rate. In light of this, we propose a new approach for estimating the phase composition and concentration of solid Ga films by fitting measured dielectric function spectra with a Bruggeman effective medium approximation using the calculated dielectric functions for the pure phases. Bearing this in mind, we have evaluated the electromagnetic response of localized and surface plasmons (LSPs and SSPs) excited in nanostructures and films of Ga polymorphs by showing their different electromagnetic behaviour from NIR to UV. The results of this research will facilitate the controllable use of Ga for phase change applications in photonics and plasmonics by allowing the desing and accurate modeling of these Ga-based active phase-change plasmonics systems. Finally, this work opens new paths for preparing “à la carte” Ga plasmonic devices.

4. Experimental Section

Ga thin film synthesis and analysis: Solid gallium samples were obtained by cooling a ~2 μm-thick liquid Ga layer deposited on a sapphire slide. The back of the sapphire slide was coated with titanium to assure good thermal contact between the Ga film, the slide, and the temperature-programmable stage. When *l*-Ga is cooled below T_m, it does not necessarily crystallize into the stable α-Ga phase; instead, polycrystalline Ga solids are obtained, and several metastable phases can be accessed.

The experimentally-controlled parameters affecting the polycrystalline structure during the cooling process were the cooling speed, the targeted final temperature, and the chamber atmosphere. The slide was positioned on a plate whose temperature could be controlled and programmed from the temperature of liquid nitrogen (-196°C) up to 300°C. The stage was in a cell purged with flowing ultrahigh purity (0.999999) N_2 to prevent condensation of water and impurities on the Ga layer.

- Sample Ga#1 was prepared by cooling to -40°C with a cooling rate of 20°C/min while flowing N_2. Sample Ga#1 was found to be a homogeneous mixture of α- and metastable β-Ga phases. This is consistent with the partial metallic bonding of the β-Ga, whose crystallization is characterized by monoatomic packing, a generally fast process.
- Sample Ga#2 was cooled to -150°C with a cooling rate of 5°C/min while flowing N_2. It was found to be a polycrystalline mixture of α- and γ-Ga phases.

The cell had optical ports and was mounted on the stage of a spectroscopic ellipsometer so that the dielectric function spectra of the cooled Ga solid films could be obtained in the spectral range 0.75 – 6.5 eV with 0.01 eV resolution (see experimental data in Figure 2). Those samples were also analyzed by low temperature x-ray diffraction (XRD) to identify the solid phase from the measured d-spacing, as shown in **Table S4**.

Computational Details Density functional first-principles calculations based on a numerical atomic orbital method were carried out using SIESTA code[31]. All the calculations have been performed with the Generalized Gradient Approximation (GGA), using the exchange-correlation potential parametrized by Perdew-Burke-Ernzerhof[42] (PBEsol) to simulate the electronic exchange and correlation.

Core electrons are described by *ab-initio* optimized norm conserving pseudopotentials, generated following the recipe given by Hamann[43], available in the PSEUDODOJO[44,45] in the Kleinman-Bylander fully non-local separable representation. The $3s$, $3p$, $3d$, $4s$ and $4p$ were considered as valence electrons of Ga and explicitly included in the calculations.

The one-electron Kohn Sham eigenvectors were expanded in a basis of localized numeric atomic orbitals (NAO) as implemented in SIESTA code. The size of the basis set chosen was single ζ for the semicore $3s$ and $3p$, double ζ for $3d$ and $4p$, and triple ζ for $4s$ orbitals. All the parameters required to describe the shape and the range of the NAO were variationally optimized following the recipe in Refs. [[46,47]] . The optimal basis set is available upon request.

The electronic density, Hartree, and exchange correlation potentials, as well as the corresponding matrix elements between the basis orbitals, were calculated in a uniform real space grid. The equivalent plane wave cut-off used to represent the charge density was 800 Ry. For the Brillouin integrations, we use a Monkhorst-Pack[48] sampling of 10×10×10 for the α-, β-, and δ-phases and 6×6×10 for the γ-phase.

For the structural characterization atoms and unit cell were allowed to relax until the maximum component of the force acting on any atoms were smaller than 0.01 eV/Å, and the maximum component of the stress tensor was smaller than 0.0001 eV/Å^3.

Optical Response: The frequency dependent optical response of the studied structures was obtained using first-order time-dependent perturbation theory to calculate the dipolar transition matrix elements between occupied and unoccupied single-electron eigenstates as implemented in SIESTA code. The optical constants of a solid can be derived from the complex dielectric function $\epsilon(\omega) = \epsilon_1(\omega) + i\epsilon_2(\omega)$. The frequency-dependent dielectric function can be written within the dipole approximation as

$$\epsilon_2(\omega) = \frac{2\pi}{mN}\frac{\omega_p^2}{\omega^2}\sum_{v,c}\int_{BZ}\frac{d\mathbf{k}}{(2\pi)^3}|M_{cv\boldsymbol{k}}|\delta(\epsilon_{c\mathbf{k}} - \epsilon_{v\mathbf{k}} - \hbar\omega)$$

where m is the electron mass, N is the number of electrons per unit volume, and $\omega_p^2 = 4\pi N e^2/m$ is the plasma frequency, with e being the electron charge. The single particle electronic states $|\psi\rangle$ of energy ε are labeled by their crystal momentum $\mathbf{k}$ and their valence v and conduction c band index. The sun is over connecting valence and conduction states and over all the $\mathbf{k}$ points in the first Brillouin zone. The optical matrix element is given by $M_{cv\boldsymbol{k}} = \langle\psi_{c\mathbf{k}}|\hat{\boldsymbol{e}}\cdot\mathbf{p}|\psi_{v\mathbf{k}}\rangle$, where $\hat{\boldsymbol{e}}$ is the polarization of the incident light and $\mathbf{p}$ is the momentum operator. The real part of the dielectric function $\epsilon_1(\omega)$ can be obtained from the imaginary part using the Kramers-Kronig relation.

In order analyze the origin of the peaks appearing in the $\epsilon_2(\omega)$ spectra due to interband transitions, we have calculated the values of the optical matrix element $M_{cv\boldsymbol{k}}$ for every pair of conduction and valence bands at each $\mathbf{k}$ point with an energy difference equal to the photon energy at which the peak appear. In this way, we can analyze the pair of bands contributing to the interband transition visible in $\epsilon_2(\omega)$ spectra.

All bands have been included in the optical calculations of each Ga phase. The optical mesh used for is 40×40×40 for the α-, β-, and δ-phases and 40×40×50 for the γ-phase. The gaussian broadening has been set to 0.20 Ry for α- and δ-phases, 0.25 Ry for β-Ga and 0.1 for γ-Ga.

Reflectance Calculations: The reflectance calculations have been performed using the Transfer Matrix Method (TMM). TMM allows the calculation of the reflectance (R), transmittance (T), and absorbance (A) spectra of an arbitrary system of homogeneous, non-magnetic multilayers.

We have considered Ga films of thicknesses h = 20 and 150 nm deposited on a sapphire substrate (refractive index n =1.78 [49]) and exposed to air. These values of h have been chosen according to typical experimental values found in the literature.[9,11] The angle between the wave-vector $\boldsymbol{k}$ and the surface's normal (AOI) has been fixed to 0° or 70°. Both s- and p-polarizations (perpendicular and parallel to the plane of incidence respectively), along with AOI, have been chosen to mimic the typical conditions for spectroscopic ellipsometry measurements.

Electromagnetic Simulations: Electromagnetic simulations have been performed using the finite difference time-domain-based software Lumerical FDTD Solutions. Total-field/scattered field light source conditions were used in all simulations. An illuminating linearly-polarized plane-wave was set to propagate perpendicular to the substrate. The wavelength spectral range analyzed was set from 200 to 1500 nm to mimic experimental conditions. A non-uniform mesh was used in the simulation region. A finer mesh was defined in the vicinity of the NP. In this region, the mesh step was fixed to d_x=d_y=d_z=1 nm. The absorption cross-section was calculated within the total-field/scattered-field formalism

Supporting Information

Supporting Information is available from the Wiley Online Library or from the author.

Acknowledgements

M.L. acknowledges the support of the European Commission under the H2020 grant TWINFUSYON (GA692034). Y.G. and F.M. acknowledges the support by the Army Research Laboratory under Cooperative Agreement Number W911NF-17-2-0023 and by SODERCAN (Sociedad para el Desarrollo de Cantabria) through the Research Vicerrectorate of the University of Cantabria. Y.G. thanks the University of Cantabria for her FPU grant. P.G.-F. and J.J. acknowledge financial support from the Spanish Ministry of Economy and Competitiveness through grant number FIS2015-64886-C5-2-P, and P.G.-F. acknowledges support from Ramón y Cajal grant no. RyC-2013-12515.

Received: ((will be filled in by the editorial staff))
Revised: ((will be filled in by the editorial staff))
Published online: ((will be filled in by the editorial staff))

References

[1] Y. Lu, Q. Hu, Y. Lin, D. B. Pacardo, C. Wang, W. Sun, F. S. Ligler, M. D. Dickey, Z. Gu, *Nat. Commun.* **2015**, *6*, 1.

[2] G. Bo, L. Ren, X. Xu, Y. Du, S. Dou, *Adv. Phys. X* **2018**, *3*, 1446359.

[3] R. W. G. Wyckoff, *Crystal Structures, Vol. 1*, Wiley, **1963**.

[4] L. Bosio, A. Defrain, H. Curien, A. Rimsky, *Acta Crystallogr. Sect. B Struct. Crystallogr. Cryst. Chem.* **1969**, *25*, 995.

[5] L. Bosio, H. Curien, M. Dupont, A. Rimsky, *Acta Crystallogr. Sect. B Struct. Crystallogr. Cryst. Chem.* **1972**, *28*, 1974.

[6] L. Bosio, H. Curien, M. Dupont, A. Rimsky, *Acta Crystallogr. Sect. B Struct. Crystallogr. Cryst. Chem.* **1973**, *29*, 367.

[7] M. Bernasconi, G. L. Chiarotti, E. Tosatti, *Phys. Rev. B* **1995**, *52*, 9988.

[8] X. G. Gong, G. L. Chiarotti, M. Parrinello, E. Tosatti, *Phys. Rev. B* **1991**, *43*, 14277.

[9] S. R. C. Vivekchand, C. J. Engel, S. M. Lubin, M. G. Blaber, W. Zhou, J. Y. Suh, G. C. Schatz, T. W. Odom, *Nano Lett.* **2012**, *12*, 4324.

[10] A. V. Krasavin, N. I. Zheludev, *Appl. Phys. Lett.* **2004**, *84*, 1416.

[11] A. V. Krasavin, A. V. Zayats, N. I. Zheludev, *J. Opt. A Pure Appl. Opt.* **2005**, *7*, S85.

[12] R. Li, L. Wang, L. Li, T. Yu, H. Zhao, K. W. Chapman, Y. Wang, M. L. Rivers, P. J. Chupas, H. Mao, H. Liu, *Sci. Rep.* **2017**, *7*, 5666.

[13] P. Ghigna, G. Spinolo, G. B. Parravicini, A. Stella, A. Migliori, R. Kofman, *J. Am. Chem. Soc.* **2007**, *129*, 8026.

[14] M. Losurdo, A. Suvorova, S. Rubanov, K. Hingerl, A. S. Brown, *Nat. Mater.* **2016**, *15*, 995.

[15] S. Pochon, K. F. MacDonald, R. J. Knize, N. I. Zheludev, *Phys. Rev. Lett.* **2004**, *92*, 145702.

[16] P. C. Wu, M. Losurdo, T.-H. Kim, S. Choi, G. Bruno, A. S. Brown, *J. Vac. Sci. Technol. B Microelectron. Nanom. Struct.* **2007**, *25*, 1019.

[17] P. C. Wu, T.-H. Kim, A. S. Brown, M. Losurdo, G. Bruno, H. O. Everitt, *Appl. Phys. Lett.* **2007**, *90*, 103119.

[18] P. C. Wu, C. G. Khoury, T.-H. Kim, Y. Yang, M. Losurdo, G. V. Bianco, T. Vo-Dinh, A. S. Brown, H. O. Everitt, *J. Am. Chem. Soc.* **2009**, *131*, 12032.

[19] A. G. Marín, T. García-Mendiola, C. N. Bernabeu, M. J. Hernández, J. Piqueras, J. L. Pau, F. Pariente, E. Lorenzo, *Nanoscale* **2016**, *8*, 9842.

[20] A. I. Denisyuk, F. Jonsson, N. I. Zheludev, in *2007 Eur. Conf. Lasers Electro-Optics Int. Quantum Electron. Conf.*, IEEE, **2007**, pp. 1–1.

[21] N. I. Zheludev, *J. Opt. A Pure Appl. Opt.* **2006**, *8*, S1.

[22] K. F. MacDonald, V. A. Fedotov, S. Pochon, G. Stevens, F. V Kusmartsev, V. I. Emel’yanov, N. I. Zheludev, *Europhys. Lett.* **2004**, *67*, 614.

[23] S. Ghosh, S. Lim, *IEEE Trans. Antennas Propag.* **2018**, *66*, 4953.

[24] V. A. Fedotov, V. I. Emel yanov, K. F. MacDonald, N. I. Zheludev, *J. Opt. A Pure Appl. Opt.* **2004**, *6*, 155.

[25] L. Comez, A. Di Cicco, J. Itié, A. Polian, *Phys. Rev. B* **2001**, *65*, 1.

[26] J. M. Sanz, D. Ortiz, R. Alcaraz de la Osa, J. M. Saiz, F. González, a. S. Brown, M. Losurdo, H. O. Everitt, F. Moreno, *J. Phys. Chem. C* **2013**, *117*, 19606.

[27] P. Albella, B. Garcia-Cueto, F. González, F. Moreno, P. C. Wu, T. H. Kim, A. Brown,

Y. Yang, H. O. Everitt, G. Videen, *Nano Lett.* **2011**, *11*, 3531.

[28] M. Yarema, M. Wörle, M. D. Rossell, R. Erni, R. Caputo, L. Protesescu, K. V. Kravchyk, D. N. Dirin, K. Lienau, F. von Rohr, A. Schilling, M. Nachtegaal, M. V. Kovalenko, *J. Am. Chem. Soc.* **2014**, *136*, 12422.

[29] D. A. G. Bruggeman, *Ann. Phys.* **1935**, *416*, 636.

[30] X. F. Li, G. T. Fei, X. M. Chen, Y. Zhang, K. Zheng, X. L. Liu, L. De Zhang, *EPL (Europhysics Lett.* **2011**, *94*, 16001.

[31] J. M. Soler, E. Artacho, J. D. Gale, A. García, J. Junquera, P. Ordejón, D. Sánchez-Portal, *J. Phys. Condens. Matter* **2002**, *14*, 2745.

[32] J. M. McMahon, G. C. Schatz, S. K. Gray, *Phys. Chem. Chem. Phys.* **2013**, *15*, 5415.

[33] G. Jezequel, J. C. Lemonnier, J. Thomas, *J. Phys. F Met. Phys.* **1977**, *7*, 1613.

[34] O. Hunderi, R. Ryberg, *J. Phys. F Met. Phys.* **1974**, *4*, 2084.

[35] P. M. Allen, in *Underst. Regres. Anal.*, Springer US, Boston, MA, **n.d.**, pp. 91–95.

[36] C. F. Bohren, D. R. Huffman, Eds. , *Absorption and Scattering of Light by Small Particles*, Wiley-VCH Verlag GmbH, Weinheim, Germany, **1998**.

[37] M. G. Blaber, M. D. Arnold, M. J. Ford, *J. Phys. Condens. Matter* **2010**, *22*, DOI: 10.1088/0953-8984/22/14/143201.

[38] M. Born, E. Wolf, A. B. Bhatia, P. C. Clemmow, D. Gabor, A. R. Stokes, A. M. Taylor, P. A. Wayman, W. L. Wilcock, *Principles of Optics*, Cambridge University Press, Cambridge, **1999**.

[39] K. F. MacDonald, V. A. Fedotov, S. Pochon, K. J. Ross, G. C. Stevens, N. I. Zheludev, W. S. Brocklesby, V. I. Emel'yanov, *Appl. Phys. Lett.* **2002**, *80*, 1643.

[40] J. Toudert, R. Serna, *Opt. Mater. Express* **2017**, *7*, 2299.

[41] Y. Yang, J. M. Callahan, T. H. Kim, A. S. Brown, H. O. Everitt, *Nano Lett.* **2013**, *13*, 2837.

[42] J. P. Perdew, A. Ruzsinszky, G. I. Csonka, O. A. Vydrov, G. E. Scuseria, L. A.

Constantin, X. Zhou, K. Burke, *Phys. Rev. Lett.* **2008**, *100*, 136406.

[43] D. R. Hamann, *Phys. Rev. B* **2013**, *88*, 085117.

[44] M. J. Van Setten, V. A. Popa, G. A. De Wijs, G. Brocks, *Phys. Rev. B - Condens. Matter Mater. Phys.* **2007**, *75*, 1.

[45] NC SR (ONCVPSP v0.4) stringent, http://www.pseudo-dojo.org/pseudos/nc-sr-04_pbesol_stringent/Ga.html.

[46] J. Junquera, Ó. Paz, D. Sánchez-Portal, E. Artacho, *Phys. Rev. B* **2001**, *64*, 235111.

[47] E. Anglada, J. M. Soler, J. Junquera, E. Artacho, *Phys. Rev. B* **2002**, *66*, 205101.

[48] H. J. Monkhorst, J. D. Pack, *Phys. Rev. B* **1976**, *13*, 5188.

[49] A. K. Harman, S. Ninomiya, S. Adachi, *J. Appl. Phys.* **1994**, *76*, 8032.

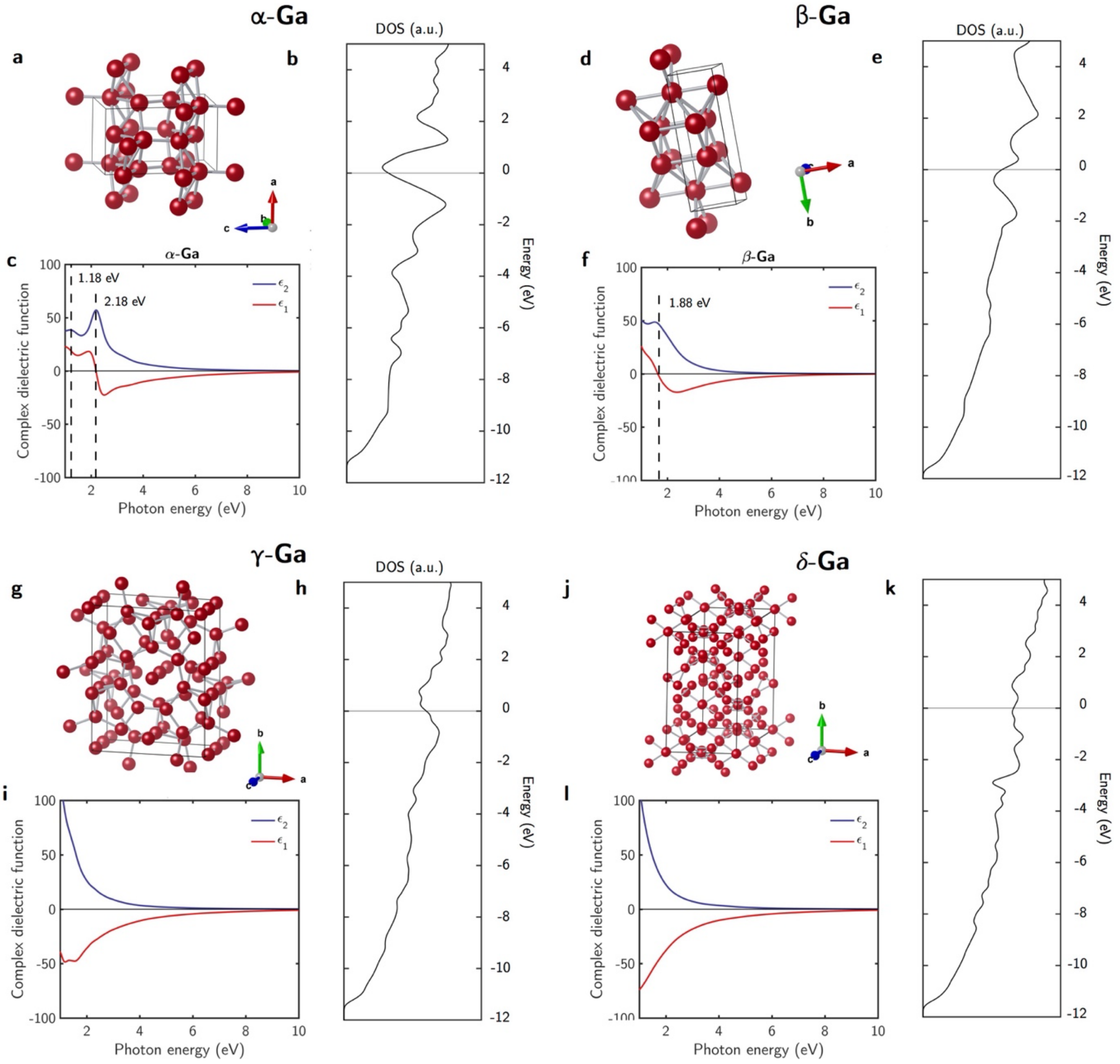

Figure 1. Unit cell, density of states (DOS), and dielectric function of the Ga phases. (**a, d, g, j**) structure of the unit cell, (**b, e, h, k**) DOS, and (**c, f, i, l**) complex dielectric function ($\epsilon = \epsilon_1 + i\epsilon_2$) of α-Ga (top left), β-Ga (top right), γ-Ga (bottom left), and δ-Ga (bottom right).

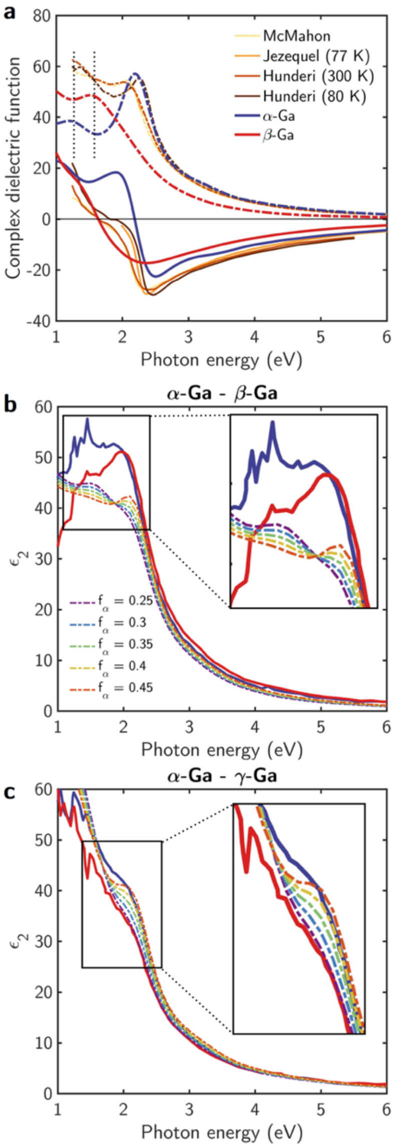

Figure 2. Comparison of measured and calculated complex dielectric functions. (**a**) Measured complex dielectric function of Ga reported by several authors,[32–34] and calculated dielectric function of α-Ga (blue curve) and β-Ga (red curve) for which continuous lines correspond to the real part of the dielectric function and dot-dashed lines correspond to its imaginary part. Ellipsometric measurements of the pseudo-dielectric function (solid lines) of samples with (**b**) α-Ga/β-Ga and (**c**) α-Ga/γ-Ga content at a 70° angle of incidence for two sample locations (red and blue curves). The dashed lines represent the Bruggeman effective dielectric functions obtained through the mixture of the corresponding theoretical dielectric functions, for which the parameter f_α represents the volume fraction of α-Ga in the sample.

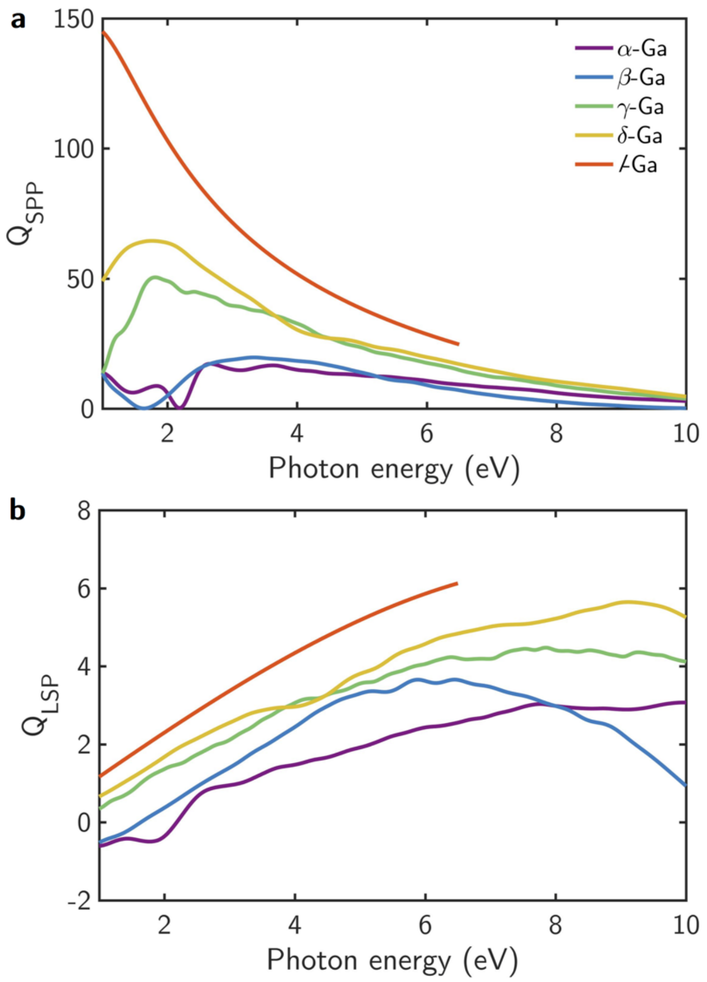

Figure 3. Simulated surface and localized surface plasmon quality factors. (**a**) Q_{SSP} and (**b**) Q_{LSP} spectra for each of the analyzed phases.

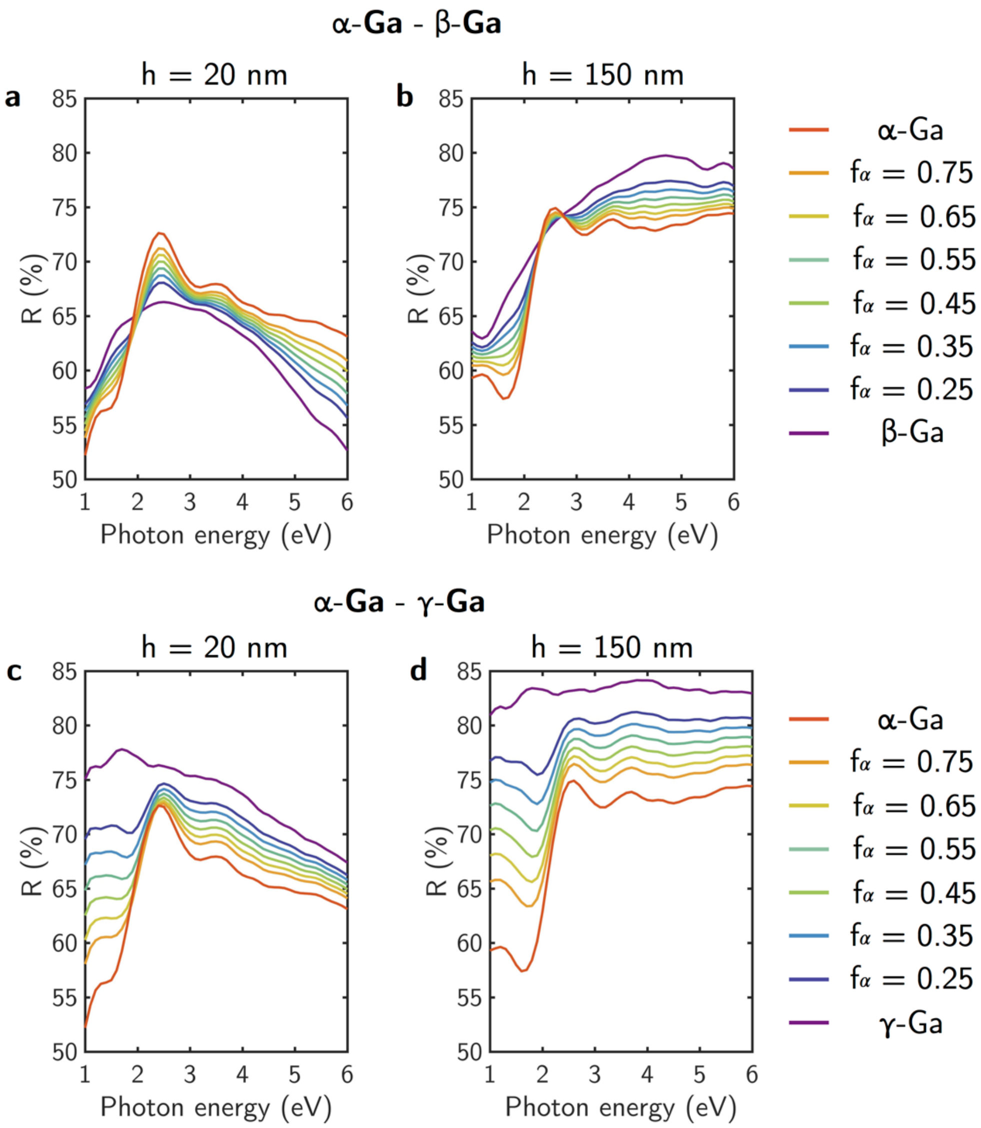

Figure 4. Simulated reflectance spectra of (**a,b**) α-Ga/β-Ga and (**c,d**) α-Ga/γ-Ga thin films on a sapphire substrate (refractive index n = 1.78). The dielectric function considered in each case is calculated through the Bruggeman effective medium approximation, with the α-phase filling fraction f_α indicated in the legend. The thin films have thicknesses of h = 20 (**a,c**) and 150 nm (**b,d**) and are illuminated at normal incidence (AOI = 0°).

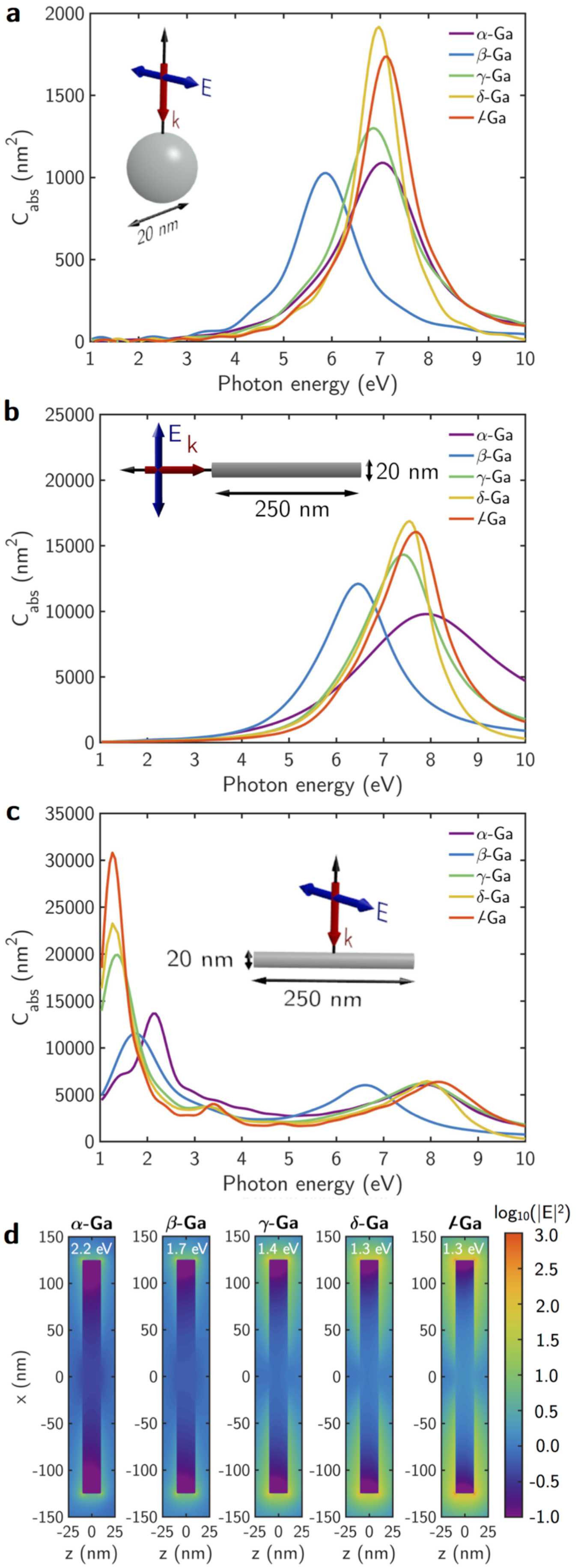
a
b
c
d
C_{abs} (nm^2)
Photon energy (eV)
α-Ga
β-Ga
γ-Ga
δ-Ga
ł-Ga
E
k
20 nm
250 nm
2000
1500
1000
500
0
25000
20000
15000
10000
5000
35000
30000
1
2
3
4
5
6
7
8
9
10
α-Ga
2.2 eV
β-Ga
1.7 eV
γ-Ga
1.4 eV
δ-Ga
1.3 eV
ł-Ga
1.3 eV
x (nm)
z (nm)
150
100
50
0
-50
-100
-150
-25
0
25
log₁₀(|E|²)
3.0
2.5
2.0
1.5
1.0
0.5
0.0
-0.5
-1.0

Figure 5. Simulated plasmonic response of Ga-phases nanospheres and nanorods. (**a**) Absorption cross-section (C_{abs}) of spherical NPs with radius R = 10 nm made of the different Ga-phases. (**b,c**) C_{abs} of nanorods of length L = 250 nm and radius R = 10 nm made of the different Ga-phases: (**b**) nanorod illuminated along its symmetry axis, and (**c**) nanorod illuminated perpedicular to its symmetry axis with polarization rotated 45º from that axis. The insets indicate the simulation geometry, with ***k*** as the propagating direction of the illuminating beam and ***E*** as the polarization vector. (**d**) Near-field enhancement ($\log_{10}(|E|^2)$) color maps of the nanorods made of each Ga-phase, excited at their low energy (longitudinal) mode.

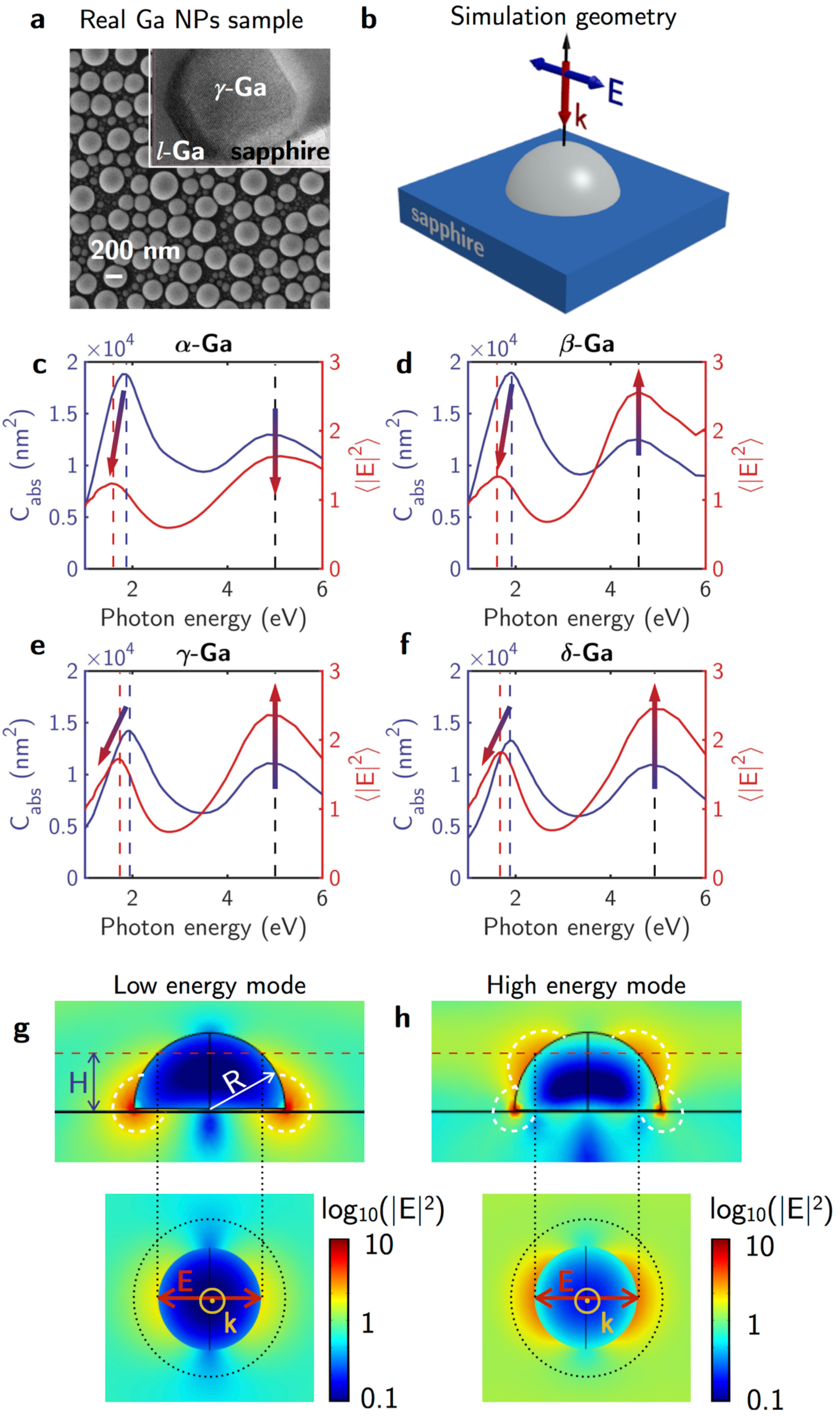
a
Real Ga NPs sample
γ-Ga
l-Ga
sapphire
200 nm
b
Simulation geometry
E
k
sapphire
c
α-Ga
d
β-Ga
e
γ-Ga
f
δ-Ga
×10^4
C_abs (nm^2)
⟨|E|^2⟩
Photon energy (eV)
0
0.5
1
1.5
2
3
4
6
g
Low energy mode
H
R
h
High energy mode
E
k
log10(|E|^2)
10
1
0.1

Figure 6. Simulated absorption cross-section and near-field enhancement on Ga-phases hemispheres. (**a**) SEM and TEM (inset) of a real sample of Ga NPs deposited on a sapphire substrate, similar to that used for prior SERS experiments[18,41]. (**b**) Geometrical scheme used for the electromagnetic simulations, mimicking the real sample: a hemipherical Ga NP on a sapphire substrate illuminated at normal incidence, where ***k*** inidcates the wave vector and ***E*** the electric field vector. Absorption cross-section (C_{abs}, blue curve) and near-field enhancement ($\langle|E|^2\rangle$, red curve) averaged over the surface of a R = 60 nm (**c**) α-Ga, (**d**) β-Ga, (**e**) γ-Ga, and (**f**) δ-Ga hemispherical NP on a sapphire substrate. Near-field distribution ($\log_{10}(|E|^2)$) of the (**g**) low and (**h**) high energy modes. The top panels show the plane containing the wave vector **k** and electric field vector **E**. The bottom panels present $\log_{10}(|E|^2)$ in a plane lifted H = 45 nm above the substrate, near where most adsorbates will attach. Although the near-field maps correspond to δ-Ga, the near-field distribution is the same for all phases.

ToC figure

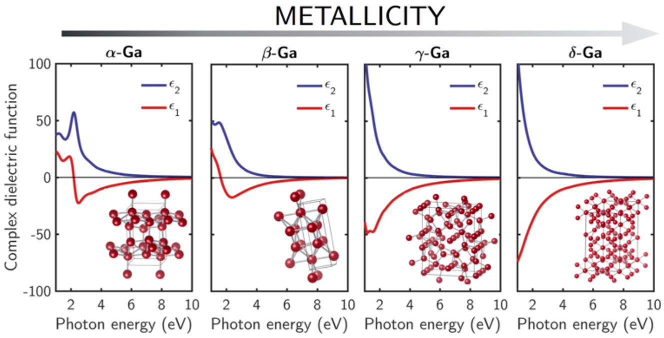

Supporting Information

GALLIUM POLYMORPHS: PHASE-DEPENDENT PLASMONICS

*Yael Gutiérrez,[1] Maria Losurdo,[2] Pablo García-Fernández, [3] Marta Sainz de la Maza[1,3], Francisco González,[1] April S. Brown,[4] Henry O. Everitt[5,6] Javier Junquera[3] and Fernando Moreno[1]**

Polymorphysm and phase diagram of gallium bulk and gallium nanoparticles

Figure S1 summarizes the various phases experimentally reported for bulk Ga (left panel) and for Ga NPs with different size deposited by different methodologies.

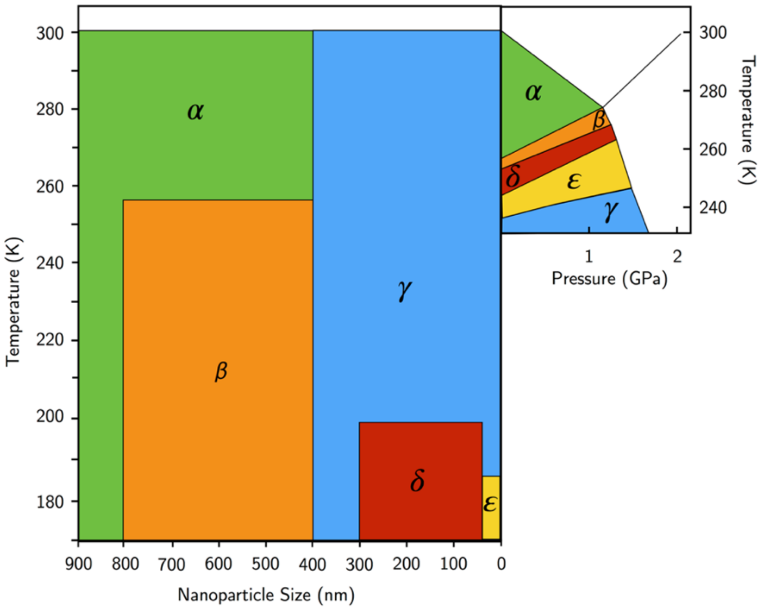

Figure S1. Phase diagram of bulk Ga from Ref [1] (right panel) and for Ga NPs (left panel), as summarized from data reported in various sources[2,3,4] showing the phases expected at the various temperatures.

---

[1] Bosio, L. Crystal structures of Ga(II) and Ga(III). *J. Chem. Phys.* **68,** 1221–1223 (1978).

[2] Losurdo, M., Suvorova, A., Rubanov, S., Hingerl, K. & Brown, A. S. Thermally stable coexistence of liquid and solid phases in gallium nanoparticles. *Nat. Mater.* **15,** 995–1002 (2016).

[3] Yarema, M. *et al.* Monodisperse Colloidal Gallium Nanoparticles: Synthesis, Low Temperature Crystallization, Surface Plasmon Resonance and Li-Ion Storage. *J. Am. Chem. Soc.* **136,** 12422–12430 (2014).

[4] Li, X. F. *et al.* Size-temperature phase diagram of gallium. *EPL (Europhysics Lett.* **94,** 16001 (2011).

Band diagram of α- and β-Ga

Band diagram of α- and β-Ga in which with arrows are indicated the interband transitions apperarig in the comples dielectric function: at 1.18 and 2.18 eV for α-Ga and at 1.88 eV for β-Ga. With a color code is represented the intensity of each of the transitions based on the evaluation of the optical matrix element ($M_{cv\boldsymbol{k}}$).

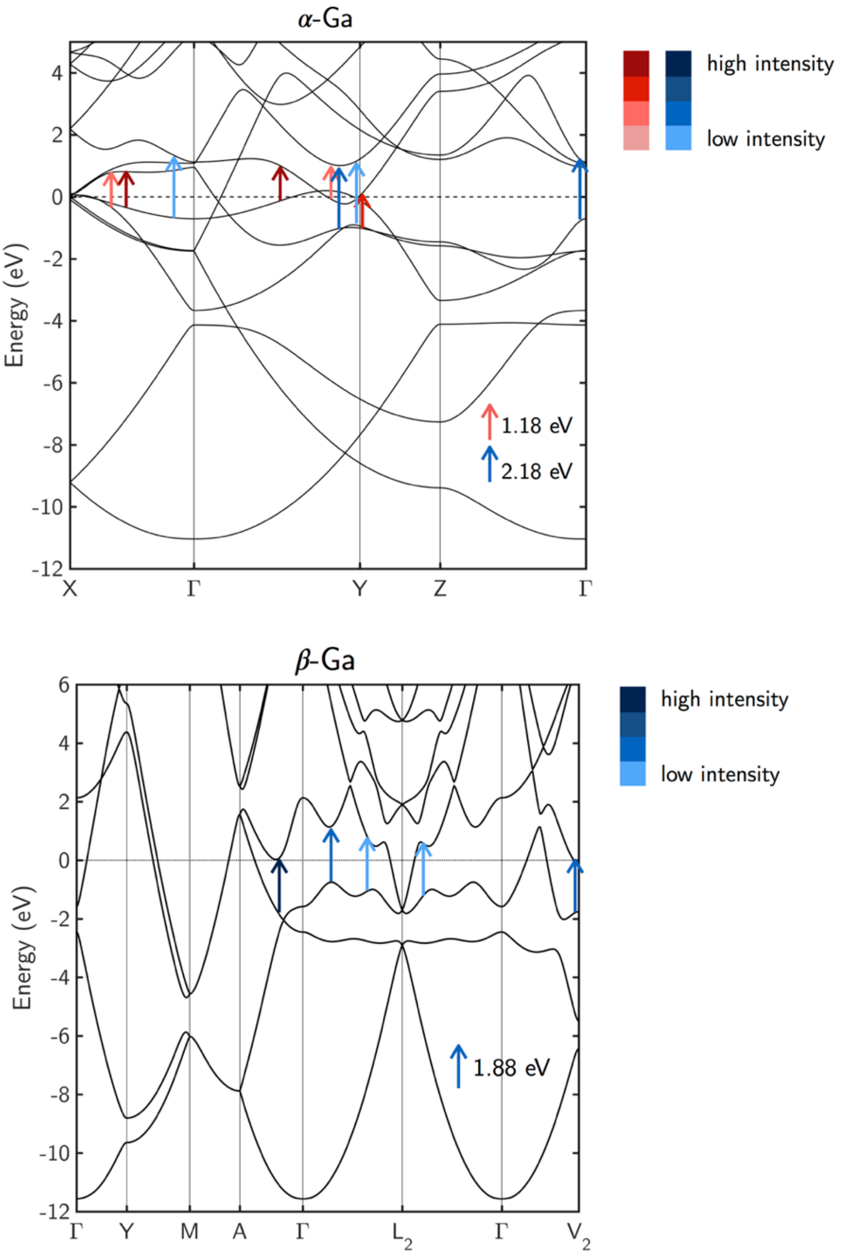

Figure S2. Band diagram of α- and β-Ga. With arrows are indicated the interband transtions appearing in the complex dielectric function of α- and β-Ga at 1.18 (red arrows) and 2.18 eV (blue arrows), and 1.88 eV (blue arrows) repectively. With a color code is represented the intensity of the transition based on the evaluation of the optical matrix element ($M_{cv\boldsymbol{k}}$).

Reflectance of Ga thin films at oblique incidence

Reflectance spectra calculated using the Transfer Matrix Method (TMM) of α-Ga/β-Ga and α-Ga/γ-Ga thin films with different content of the α-phase at oblique incidence AOI =70° with *s*- and *p*-polarization.

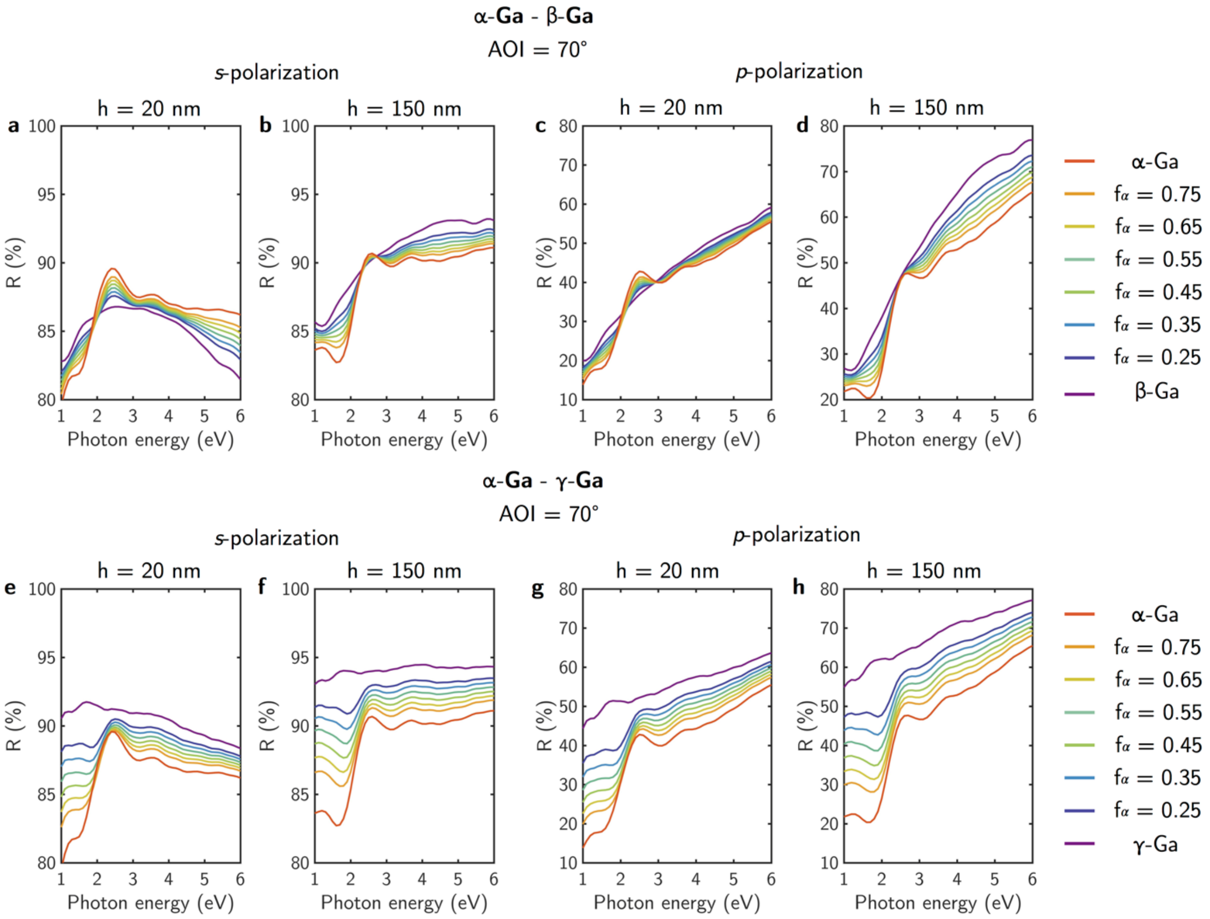

Figure S3. Reflectance spectra (*R*) of (**a-d**) α-Ga/β-Ga and (**e-h**) α-Ga/γ-Ga thin films on a sapphire substrate (refractive index n = 1.78). The dielectric function considered in each case is calculated through the Bruggeman effective medium approximation with a filling fraction of the α-phase f_α indicated in the legend. The thin films have thicknesses of *h* = 20 (**a,c,e,g**) and 150 nm (**b,d,f,h**) and are illuminated at oblique incidence (AOI = 70) with *s*- (**a,b,e,f**) and *p*-polarization (**c,d,g,h**).

Table S1. Theoretical lattice constants, structural parameters and atomic coordinates of α-Ga, β-Ga, γ-Ga, and δ-Ga. Some experimental values are added for reference.

α-Ga			β-Ga		
Property	This work	Experiment[5]	Property	This work	Experiment[6]
Lattice parameters			Lattice parameters		
|a|(Å)	4.528	4.511	|a|(Å)	2.777	2.766
|b|(Å)	4.494	4.517	|b|(Å)	8.062	8.053
|c|(Å)	7.645	7.645	|c|(Å)	3.215	3.332
$\boldsymbol{\theta}_{\mathrm{bc}}$ (°)	90.00	90.00	$\boldsymbol{\theta}_{\mathrm{bc}}$ (°)	90.00	90.00
$\boldsymbol{\theta}_{\mathrm{ac}}$ (°)	90.00	90.00	$\boldsymbol{\theta}_{\mathrm{ac}}$ (°)	90.01	92.03
$\boldsymbol{\theta}_{\mathrm{ab}}$ (°)	90.00	90.00	$\boldsymbol{\theta}_{\mathrm{ab}}$ (°)	90.00	90.00
Coordinates (Å)			Coordinates (Å)		
x_{GaI}	2.2639	2.2553	x_{GaI}	1.4044	1.3830
y_{GaI}	0.3737	0.3544	y_{GaI}	2.9525	2.9715
z_{GaI}	5.0118	4.9882	z_{GaI}	2.4377	2.4990

γ-Ga			δ-Ga		
Property	This work	Experiment[7]	Property	This work	Experiment[8]
Lattice parameters			Lattice parameters		
|a|(Å)	10.540	10.593	|a|(Å)	9.063	9.087
|b|(Å)	13.395	13.523	|b|(Å)	9.063	9.087
|c|(Å)	5.178	5.203	|c|(Å)	16.869	17.020
$\boldsymbol{\theta}_{\mathrm{bc}}$ (°)	90.00	90.00	$\boldsymbol{\theta}_{\mathrm{bc}}$ (°)	90.00	90.00
$\boldsymbol{\theta}_{\mathrm{ac}}$ (°)	90.00	90.00	$\boldsymbol{\theta}_{\mathrm{ac}}$ (°)	90.00	90.00
$\boldsymbol{\theta}_{\mathrm{ab}}$ (°)	90.00	90.00	$\boldsymbol{\theta}_{\mathrm{ab}}$ (°)	120.00	120.00
Coordinates (Å)			Coordinates (Å)		
x_{GaI}	0.0000	0.0000	x_{GaI}	0.0000	0.0000
y_{GaI}	0.0072	0.0121	y_{GaI}	0.0000	0.0000
z_{GaI}	1.2945	1.3007	z_{GaI}	0.0000	0.0000
x_{GaII}	2.9245	2.9596	x_{GaII}	1.3082	1.3111
y_{GaII}	0.6974	0.6815	y_{GaII}	2.2655	2.2717
z_{GaII}	1.2945	1.3007	z_{GaII}	5.6231	5.6733
x_{GaIII}	0.0000	0.0000	x_{GaIII}	2.5175	2.5156
y_{GaIII}	5.2779	5.3375	y_{GaIII}	0.0000	0.0000
z_{GaIII}	0.0171	0.0000	z_{GaIII}	1.0720	1.0847
x_{GaIV}	1.3144	1.3304	x_{GaIV}	0.7896	0.7948
y_{GaIV}	2.7618	2.7884	y_{GaIV}	1.3671	1.3766
z_{GaIV}	1.2945	1.3007	z_{GaIV}	3.0256	3.0142
x_{GaV}	2.4064	2.4173	x_{GaV}	1.8222	1.8283
y_{GaV}	1.8628	1.8769	y_{GaV}	3.1561	3.1790
z_{GaV}	-1.2945	-1.3007	z_{GaV}	1.5082	1.5261
x_{GaVI}	0.0000	0.0000			
y_{GaVI}	2.8624	2.9033			
z_{GaVI}	-1.2945	-1.3007			

---

[5] Wyckoff, R. W. G. *Crystal Structures, Vol. 1*. (Wiley, 1963).

[6] Bosio, L., Defrain, A., Curien, H. & Rimsky, A. Structure cristalline du gallium β. *Acta Crystallogr. Sect. B Struct. Crystallogr. Cryst. Chem.* **25,** 995–995 (1969).

[7] Bosio, L., Curien, H., Dupont, M., & Rimsky, A. Structure cristalline de Gaγ. *Acta Crystallogr. Sect. B Struct. Crystallogr. Cryst. Chem.* **28,** 1974 (1972).

[8] Bosio, L., Curien, H., Dupont, M., & Rimsky, A. Structure cristalline de Gaδ. *Acta Crystallogr. Sect. B Struct. Crystallogr. Cryst. Chem.* **29,** 367-368 (1973).

Table S2. R-square coefficient of determination for fitting the experimental values with the imaginary part of the dielectric constant of α-Ga/β-Ga (sample Ga#1) and α-Ga/γ-Ga (sample Ga#2) to those calculated through Brueggemann EMT using a filling fraction of the α-phase f_α. These fittings are shown in Figures 2b and 2c in the main text.

	α-Ga/β-Ga (sample Ga#1)		α-Ga/γ-Ga (sample Ga#2)	
f_α	Blue experimental curve	Red experimental curve	Blue experimental curve	Red experimental curve
0.25	0.8878	0.8415	0.9445	0.9331
0.30	0.9154	0.8704	0.9464	0.9424
0.35	0.9377	0.8936	0.9471	0.9501
0.40	0.9553	0.9114	0.9464	0.9563
0.45	0.9681	0.9241	0.9446	0.9609

Table S3. R-square coefficient of determination for fitting the experimental values with the imaginary part of the dielectric constant of sample Ga#1 and sample Ga#2 with those calculated through a weighted average of α-Ga and *l*-Ga using a filling fraction of the α-phase f_α. This methodology is used in Ref. [24] to model the dielectric function of solid Ga.

	α-Ga/*l*-Ga (sample Ga#1)		α-Ga/*l*-Ga (sample Ga#2)	
f_α	Blue experimental curve	Red experimental curve	Blue experimental curve	Red experimental curve
0.10	0.5549	0.3170	0.7509	0.8011
0.20	0.6481	0.4590	0.8185	0.8704
0.30	0.7255	0.5817	0.8696	0.9192
0.40	0.7874	0.6850	0.9044	0.9478
0.50	0.8335	0.7689	0.9227	0.9559
0.60	0.8640	0.8335	0.9245	0.9437
0.70	0.8789	0.8787	0.9099	0.9112
0.80	0.8781	0.9046	0.8790	0.8583
0.90	0.8616	0.9111	0.8315	0.7851

Table S4. Measured d-spacings for Ga samples, and d-spacings from ICSD database. The color of the d-spacings in the Ga#1 and Ga#2 columns indicate to which Ga phase is assigned (red for α-Ga, green for β-Ga and blue for γ-Ga)

Measured Ga#1 d-spacings (Å)	Measured Ga#2 d-spacings (Å)	α-Ga orthorhombic *Bmab* no 64	β-Ga monoclinic *C2/c* no 12	γ-Ga orthorhombic *Cmca* no 63	Ga orthorhombic *Cmca* no 63
		a = 4.519 Å b = 4.526 Å c = 7.658 Å	a = 2.776 Å b = 8.053 Å c = 3.332 Å	a = 10.593 Å b = 13.523 Å c = 5.203 Å	a = 2.90 Å b = 8.13 Å c = 3.17 Å
3.759	3.819	3.82900	4.02650 (020)	5.29650 (200)	4.06700
2.934	2.946	2.95093	3.33200 (001)	4.41400 (1-11)	2.73158
2.603	2.712	2.92323	2.61452 (110)	2.77970 (330)	2.50023
2.243	2.652	2.26300	2.56608 (021)	2.62053 (150)	2.06931
1.941	2.502	2.25950	2.01325 (040)	2.60152 (002)	2.03350
1.915	2.253	1.99501	1.92575 (1-30)	2.49938 (241)	1.98054
1.755	1.985	1.95632	1.66495 (002)	2.48346 (112)	1.71161
1.645	1.991	1.94819	1.64950 (131)	1.98476 (351)	1.67967
1.390		1.94595	1.39200 (1-50)	1.85585 (402)	1.58500
		1.91450			1.47681
		1.78772			1.45000
		1.76324			1.36579
		1.59894			1.35567
					1.29502